Journal of Power Sources 196 (2011) 9998–10009

Contents lists available at ScienceDirect

Journal of Power Sources

journal homepage: www.elsevier.com/locate/jpowsour

Development and design of experiments optimization of a high temperature proton exchange membrane fuel cell auxiliary power unit with onboard fuel processor

Jörg Karstedt[a,*], Jürgen Ogrzewalla[a], Christopher Severin[a], Stefan Pischinger[b]

[a] FEV Motorentechnik GmbH, Neuenhofstrasse 181, D-52078 Aachen, Germany
[b] Institute for Combustion Engines, RWTH Aachen University, Schinkelstrasse 8, D-52062 Aachen, Germany

ARTICLE INFO

Article history:
Received 26 April 2011
Received in revised form 8 June 2011
Accepted 10 July 2011
Available online 20 July 2011

Keywords:
HT-PEM
Auxiliary power unit
CO poisoning
Autothermal fuel processor
Temperature and concentration profiles
DOE

ABSTRACT

In this work, the concept development, system layout, component simulation and the overall DOE system optimization of a HT-PEM fuel cell APU with a net electric power output of 4.5 kW and an onboard methane fuel processor are presented.

A highly integrated system layout has been developed that enables fast startup within 7.5 min, a closed system water balance and high fuel processor efficiencies of up to 85% due to the recuperation of the anode offgas burner heat. The integration of the system battery into the load management enhances the transient electric performance and the maximum electric power output of the APU system.

Simulation models of the carbon monoxide influence on HT-PEM cell voltage, the concentration and temperature profiles within the autothermal reformer (ATR) and the CO conversion rates within the watergas shift stages (WGSs) have been developed. They enable the optimization of the CO concentration in the anode gas of the fuel cell in order to achieve maximum system efficiencies and an optimized dimensioning of the ATR and WGS reactors.

Furthermore a DOE optimization of the global system parameters cathode stoichiometry, anode stoichiometry, air/fuel ratio and steam/carbon ratio of the fuel processing system has been performed in order to achieve maximum system efficiencies for all system operating points under given boundary conditions.

© 2011 Elsevier B.V. All rights reserved.

1. Introduction

The application of compact fuel cell systems as range extenders for battery electric vehicles or auxiliary power units (APUs) for onboard electric power generation enables a significant reduction of carbon dioxide and other pollutant emissions and has an improved NVH (noise vibration and harshness) performance compared to combustion-engine based technologies. Integrated fuel processing systems enable the utilization of the existing fuel infrastructure and have handling and packaging advantages over hydrogen based systems. The successful adoption of fuel cell APUs in mobile applications depends on further technological development and cost optimization of the system components and the overall system. The applications require fast startup-times, a good cyclability, a compact system design and a minimized system complexity to reduce control effort and overall system cost.

Within this work, the development of a HT-PEM fuel cell APU system with onboard fuel processor is presented. Concept development, system layout, component simulation and overall DOE (design of experiments) system optimization for maximum efficiencies are described in detail. The system is operated on natural gas and has an electric net power output of 4.5 kW. Low pollutant and noise emissions as well as a high tolerance against vibrations and a high specific system power density are important criteria for the application in an inner-city light duty delivery vehicle.

2. HT-PEM fuel cell APU concept development

For the APU development a HT-PEM fuel cell with H_3PO_4/PBI membrane was chosen because of its high resistance against shock and vibration loads of the mobile application as well as shorter startup times and improved thermal cyclability compared to solid oxide fuel cells. Advantages over LT-PEM based systems are the increased CO tolerance that significantly reduces the complexity of the fuel processing system as well as the omission of anode and cathode humidification that, in turn, enables a compact system design. The achievable cell voltages of today's state-of-the-art HT-PEM fuel cells are somewhat lower compared to LT-PEM and solid oxide fuel cells (compare Fig. 1). This can be compensated by

* Corresponding author. Tel.: +49 241 5689 9824; fax: +49 241 5689 9658.
E-mail address: Karstedt@fev.com (J. Karstedt).

0378-7753/$ – see front matter © 2011 Elsevier B.V. All rights reserved.
doi:10.1016/j.jpowsour.2011.07.034

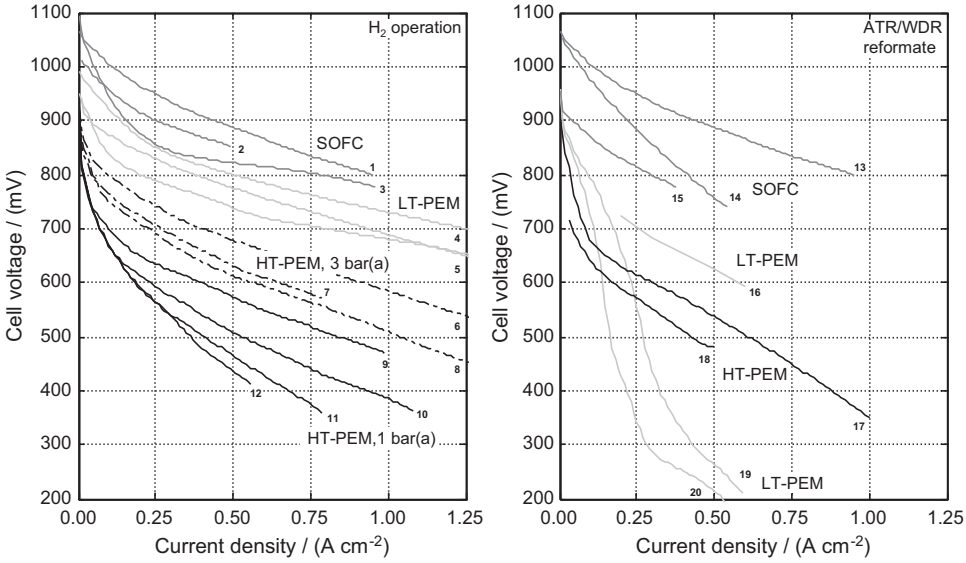

Fig. 1. Current/voltage characteristics of different LT-PEM, HT-PEM and solid oxide fuel cells for hydrogen operation and steam reforming/autothermal reformate operation (operating parameters and references are listed in the appendix (Fig. 16)).

a reduction of the targeted current density but results in a tradeoff concerning packaging volume and fuel cell cost.

In order to generate hydrogen rich synthesis gas for the fuel cell from a hydrocarbon fuel source, three main technologies are used for stationary and mobile applications:

- steam reforming (SR), where hydrocarbons and steam react endothermally to synthesis gas
- catalytic partial oxidation (CPO), where synthesis gas is produced via an exothermal partial combustion reaction of hydrocarbons and oxygen/air and
- autothermal reforming (ATR), which is a combination of exothermal CPO and endothermal SR and enables a closed heat balance of the reactor without any additional heat supplied to or dissipated from the reactor.

For the APU application autothermal reforming was selected due to packaging and transient performance advantages over steam reforming and better durability as well as reduced coke formation tendency compared to partial oxidation.

On the cathode side of the fuel cell, an increase in fuel cell efficiency, especially at high current densities, can be achieved by operating the system at elevated pressure levels. The higher power densities that can be realized for pressurized operation of the fuel cell result in a reduction of stack volume, active cell area and thus fuel cell cost. However, a high compressor efficiency and, possibly, also an expansion turbine are required to minimize the required compressor power input and to enable a net system efficiency gain. Therefore, for APU systems in a power range of 5 kW_{el}, low pressure air supply systems operating close to ambient pressure are better suited due to lower system complexity, less control effort, reduced noise emissions and reduced air supply system cost.

In conclusion, for the development of a fuel cell system with an integrated fuel processor for mobile applications that require intermittent system operation, a HT-PEM fuel cell with an autothermal fuel processor and a low pressure air supply system enables the highest degree of performance concerning the requirements system complexity, packaging, degradation, NVH and startup time/transient performance. It is selected as the basic concept for the system development presented in this paper.

2.1. System layout

The system layout of the HT-PEM APU system is presented in Fig. 2. Similar pressure losses of cathode and anode/fuel processing system facilitate the utilization of only one side channel blower in combination with an air metering device and enable packaging as well as cost advantages.

The autothermal reformer is combined with a 2-stage watergas shift CO cleanup unit enabling carbon monoxide outlet concentrations of <0.7%, that result in only a minor decrease of the HT-PEM performance at stack temperatures of 160 °C. The HT-PEM stack is liquid cooled for fast and efficient startup and compact design. It features bypass-valves that enable a disconnection of the anode and cathode during startup/shutdown to prevent condensation of water within the fuel cell. A fuel cell management system has been developed that enables the measurement of cell voltages and pressures/temperatures, it monitors fuel cell stack performance and safety and has outputs for system actuators like the air supply system, valves and relays. The combined startup-/offgas burner preheats the fuel processing system and the HT-PEM stack during startup. It converts the remaining hydrogen in the anode offgas during system operation. The heat can be recuperated for the fuel processing system. A low temperature coolant circuit is utilized to condense water from the offgas burner exhaust to enable a closed system water balance and to cool the power electronics. Two controlled DC/DC converters for auxiliaries and load enable the integration of the system battery into the load management to enhance transient performance and maximum power output of the APU system.

2.2. Global system parameters

Four global system parameters can be defined for the HT-PEM APU system, which affect system layout and system operation: the anode stoichiometry, the cathode stoichiometry, the steam/carbon ratio of the fuel processor and the air/fuel ratio of the fuel processor. For all load conditions, those parameters can be varied

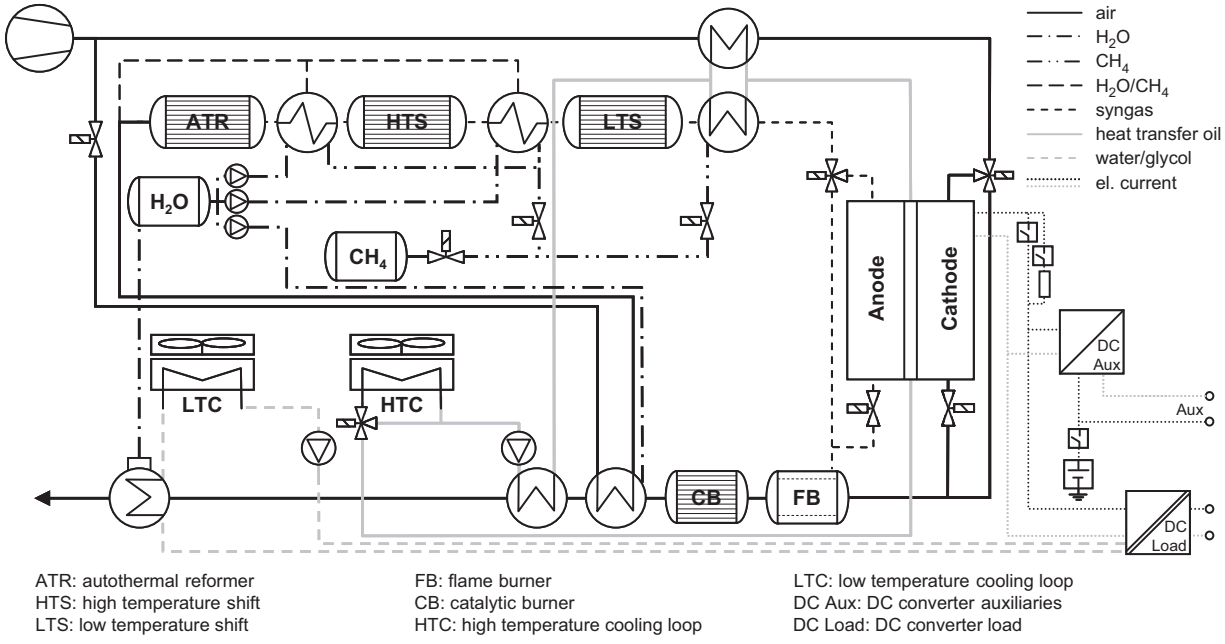

Fig. 2. System layout of the HT-PEM fuel cell APU.

within given boundaries (max. component temperatures, required heat flows, limitations of the chemical reactions e.g. by the soot limit or required conversion rates) to achieve maximum system efficiency (cf. chapter 4). The global system parameters result in massflow, pressure loss, operating temperature and gas concentration requirements for the subsystems and can be defined as follows:

2.2.1. Anode stoichiometry φ_{an}

The anode stoichiometry φ_{an} is equal to the hydrogen massflow at the anode inlet $\dot{m}_{H_2,an}$ divided by the hydrogen massflow that is converted within the fuel cell stack $\dot{m}_{H_2,an,st.}$. For a given fuel processor efficiency η_{ref} this ratio is directly proportional to the thermal power input into the fuel processor P_{ref} divided by the stack current I_{sta}.

$$\varphi_{an} = \frac{\dot{m}_{H_2,an}}{\dot{m}_{H_2,an,st.}} = \frac{\dot{m}_{H_2,an}}{x(I_{sta}/2F)M_{H_2}} \sim \frac{\eta_{ref}P_{ref}}{I_{sta}} \quad (1)$$

2.2.2. Cathode stoichiometry λ_{cat}

The cathode stoichiometry λ_{cat} is equal to the air massflow at the cathode inlet $\dot{m}_{air,cat}$ divided by the air massflow that is required for hydrogen conversion within the fuel cell stack $\dot{m}_{air,cat,st.}$.

$$\lambda_{cat} = \frac{\dot{m}_{air,cat}}{\dot{m}_{air,cat,st.}} = \frac{\dot{m}_{air,cat}}{x(I_{sta}/4F)(M_{O_2}/\xi_{O_2,air})} \sim \frac{\dot{m}_{air,cat}}{I_{sta}} \quad (2)$$

2.2.3. Air/fuel ratio fuel processing system λ_{ref}

The air/fuel ratio of the fuel processing system λ_{ref} is equal to the molar oxygen flow at the fuel processor inlet $\dot{n}_{O_2,ref}$ divided by the molar oxygen flow required stoichiometrically for total oxidation of the supplied hydrocarbon fuel $\dot{n}_{O_2,ref,st.}$.

$$\lambda_{ref} = \frac{\dot{n}_{O_2,ref}}{\dot{n}_{O_2,ref,st.}} = \frac{\dot{n}_{O_2,ref}}{(x+(y/4))\dot{n}_{C_xH_y,ref}} = \frac{\dot{n}_{O_2,ref}}{2\dot{n}_{CH_4,ref}} \quad (3)$$

2.2.4. Steam/carbon ratio fuel processing system χ_{ref}

The steam/carbon ratio of the fuel processing system is equal to the molar flow of water supplied to the fuel processor $\dot{n}_{H_2O,ref}$ divided by the molar flow of carbon supplied to the fuel processor via the hydrocarbon fuel $x\dot{n}_{C_xH_y,ref}$.

$$\chi_{ref} = \frac{\dot{n}_{H_2O,ref}}{x\dot{n}_{C_xH_y,ref}} = \frac{\dot{n}_{H_2O,ref}}{\dot{n}_{CH_4,ref}} \quad (4)$$

2.3. Subsystems

2.3.1. HT-PEM fuel cell

For a given membrane electrode assembly (MEA) and a defined stack and flowfield design, power density as well as cell voltage, thus stack efficiency, are determined by the operating parameters: stack temperature, current density, CO concentration and anode-/cathode stoichiometry. The maximum stack temperature is defined by MEA degradation and thermal stability of the selected stack materials. The current density at the nominal operating point depends on packaging and cost restrictions for the fuel cell stack. Carbon monoxide concentration and anode-/cathode stoichiometry have to be optimized on system level to maximize the net APU efficiency: cell efficiency is reduced for increasing CO concentrations due to adsorption of carbon monoxide on the platinum catalyst. However, the fuel processor efficiency increases for higher CO-concentrations. Concentration losses of the fuel cell stack are decreased at higher stoichiometries of the anode and cathode (Fig. 3), though on system level the power input of the air supply and the fuel processing system increases.

2.3.2. Fuel processing system

The fuel processing system consists of an autothermal reformer and two watergas shift (WGS) stages that reduce the carbon monoxide concentration of the synthesis gas to approx. 0.7%. The operating range of the fuel processing system parameters χ_{ref} and λ_{ref} is defined by the soot limit, the maximum catalyst temperature, the minimum required CH_4 conversion rate and the maximum CO outlet concentration of the ATR (for a given watergas shift layout). Operating boundaries can be determined with an equilibrium calculation of reactor temperature and gas concentration by assuming an adiabatic reactor and a given inlet temperature (Fig. 4).

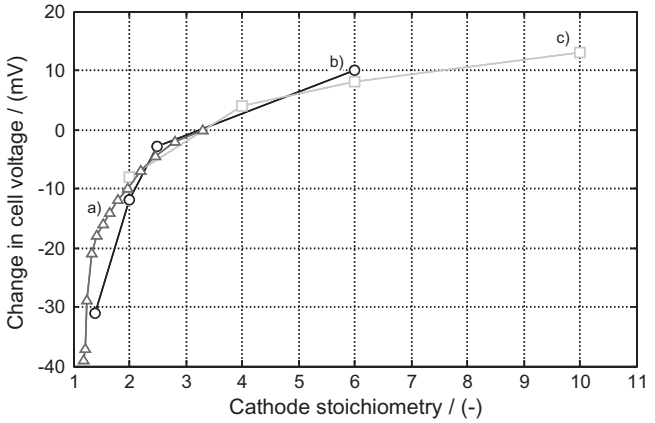

Fig. 3. Influence of cathode stoichiometry on cell voltage (a) H_3PO_4/PBI, 1 bar abs., 160 °C, reformate/air, anode stoich. 1.25, current density 0.4 A cm^{-2}, CO 0.7%, own data; (b) [1]; (c) [2].

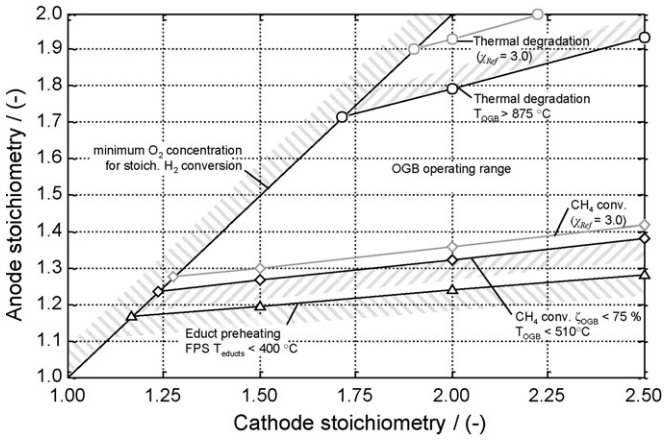

Fig. 5. Operating map of the anode offgas burner (complete oxidation of H_2 and CO, inlet temperature 160 °C, χ_{ref} = 1.5).

2.3.3. Startup/offgas burner

The combined startup/offgas burner consists of a catalytic burner for conversion of the anode offgas during system operation and a flame burner for preheating of the system during startup. With the flame burner, the system can be preheated within 7.5 min. During system operation, the operating range of the anode offgas burner is defined by the minimum oxygen concentration that is required for total oxidation of the anode offgas hydrogen content, the thermal degradation limit of the catalyst at high anode stoichiometries and the minimum required temperature for methane conversion and preheating of the reactants. With an increasing steam/carbon ratio of the fuel processor, the operating range shifts to higher anode ratios due to an increased inert gas content in the anode offgas (Fig. 5).

2.3.4. Air supply

The decrease in cell voltage due to the power consumption of the air supply system can be determined with the cathode stoichiometry λ_{cat}, the pressure ratio of the compressor Π, the compressor inlet temperature T'_{comp} and the overall compressor efficiency η_{comp} (product of isentropic, mechanical and electrical efficiency).

$$\Delta U_{cell} = \frac{\lambda M_{O_2} c_p T'_{comp} (\prod^{\kappa-1/\kappa} - 1)}{0,232 \times 4F\eta_{comp}} \quad (5)$$

Due to similar pressure losses of cathode and anode/fuel processing system, one air supply system is used. The air metering device for the anode/fuel processor air massflow has to ensure a high control accuracy of ±1% of the total air massflow in order to prevent fluctuations of the ATR temperature, which strongly depends on the air/fuel ratio of the fuel processing system.

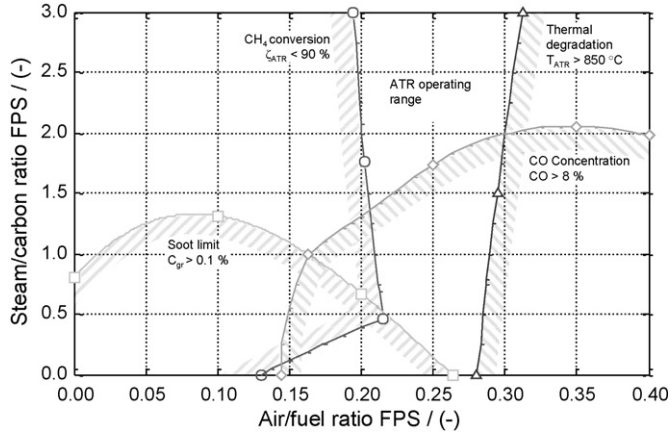

Fig. 4. Operating map of the autothermal fuel processor (equilibrium calculation, educt temperature 500 °C).

2.3.5. Cooling system

A low temperature coolant circuit is used in order to cool the power electronics and to condense water from the APU system's exhaust and enable a closed system water balance. The steam partial pressure in the anode offgas burner exhaust depends on the steam/carbon ratio χ_{ref} and the air/fuel ratio of the fuel processor λ_{ref}, the cathode stoichiometry λ_{cat} and the stack current I_{sta}:

$$p_{H_2O} = \frac{2 + \chi_{ref}}{1 + \chi_{ref} + (2\lambda_{ref} + x\lambda_{cat}(I_{sta}/4F))(1 + (\psi_{N_2,air}/\psi_{O_2,air}))} p_{amb} \quad (6)$$

In order to enable a closed system water balance, the maximum water content in the APU exhaust gas has to match the amount of product water that is generated within the fuel processor, the fuel cell stack and the anode offgas burner during the methane oxidation. Therefore, the maximum steam partial pressure in the APU system's exhaust is independent from the steam/carbon ratio of the fuel processor:

$$p_{H_2O,exh,max} = \frac{2}{1 + (2\lambda_{ref} + x\lambda_{cat}(I_{sta}/4F))(1 + (\psi_{N_2,air}/\psi_{O_2,air}))} p_{amb} \quad (7)$$

The amount of heat that has to be rejected from the low temperature coolant circuit, however, depends on the steam/carbon ratio of the fuel processing system and can amount to up to 25% of the thermal methane input power of the APU system (λ_{ref} = 0.27; ψ_{CO} = 0.5%; χ_{ref} = 3).

The high temperature coolant circuit is operated at temperatures of up to 160 °C with heat transfer oil and is used for preheating of the stack during startup as well as heat rejection from the stack and conditioning of the anode and cathode feed streams during operation.

2.4. Influence of the global system parameters on the different subsystems

The influence of the global system parameters on the different subsystems is listed in Table 1.

Table 1
Influence of the global system parameters anode stoichiometry, cathode stoichiometry, air/fuel ratio fuel processing system and steam/carbon ratio fuel processing system on the subsystems of the APU (Opt.: there exists an optimum within the variation range of the parameter).

	$\varphi_{an}\uparrow$	$\lambda_{cat}\uparrow$	$\chi_{ref}\uparrow$	$\lambda_{ref}\uparrow$
Input power compressor	↑	↑	↑	↑
Max. temperature fuel processing system	↔	↔	↓	↑
Methane conversion fuel processing system	↓	↔	Opt.	↑
Efficiency fuel processing system	↓	↔	Opt.	Opt.
Efficiency stack	↑	↑	↑	↓
Temperature/methane conversion anode offgas burner	↑	↓	↓	↔
Rejected heat HT coolant circuit	↑	↓	↔	↑
Rejected heat LT coolant circuit	↔	↑	↑	↔

Fig. 6 shows the realized HT-PEM fuel cell APU demonstrator system with integrated fuel processor.

3. Simulation

Simulation based analyses of the HT-PEM fuel cell, the autothermal reformer, the watergas shift stages and the overall APU system enable an optimized dimensioning of individual components. Further, the simulations help limit component degradation through a detailed understanding of component temperature profiles and the optimization of the global system parameters to achieve maximum system efficiencies for given boundary conditions.

3.1. HT-PEM simulation

The influence of the carbon monoxide concentration on cell voltage and efficiency of the HT-PEM stack is a key parameter for system optimization. Due to decreasing stack performance but increasing efficiencies of the fuel processing system for higher CO concentrations, an optimum carbon monoxide concentration exists, for which maximum system efficiencies are achieved.

For low temperature PEM fuel cells, a number of publications are published that describe the adsorption of carbon monoxide on the platinum catalysts and the resulting decrease of free catalyst sites that are available for the hydrogen oxidation reaction [3–7]. In order to model the influence of carbon monoxide on the HT-PEM fuel cell, the approach of Baschuk and Li [8] is adapted to determine the anodic overpotential due to carbon monoxide poisoning for the HT-PEM fuel cell.

The reaction kinetics, occurring within the anode catalyst layer, include adsorption, desorption and electrooxidation of hydrogen and carbon monoxide:

$$H_2 + 2M \underset{b_{H,ads}k_{H,ads}}{\overset{k_{H,ads}}{\rightleftarrows}} 2(H-M) \tag{8}$$

$$CO + M \underset{b_{CO,ads}k_{CO,ads}}{\overset{k_{CO,ads}}{\rightleftarrows}} CO-M \tag{9}$$

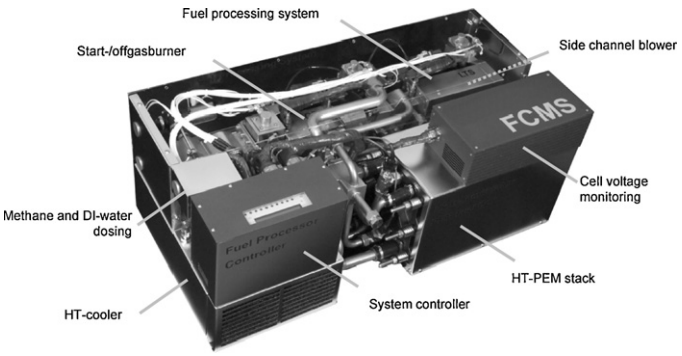

Fig. 6. HT-PEM APU demonstrator.

$$2(H-M) \xrightarrow{k_{H,ox}} 2M + 2H^+ + 2e^- \tag{10}$$

$$CO-M + H_2O \xrightarrow{k_{CO,ox}} M + CO_2 + 2H^+ + 2e^- \tag{11}$$

For the rate equations, a Langmuir kinetic is used for the adsorption and desorption of hydrogen:

$$r_{H,ads} = k_{H,ads}c_{H_2}(1-\Theta_H-\Theta_{CO})^2 - b_{H,ads}k_{H,ads}(\Theta_H)^2 \tag{12}$$

For the adsorption and desorption of CO an influence of the carbon monoxide coverage on the adsorption enthalpy is observed so that the adsorption can be described with a Temkin kinetic [9]:

$$\wedge r_{CO,ads} = k_{CO,ads}c_{CO}(1-\Theta_H-\Theta_{CO}) \quad \exp\left(-\frac{\beta\gamma\Theta_{CO}}{RT}\right) - b_{CO,ads}k_{CO,ads}\Theta_{CO} \quad \exp\left(\frac{[1-\beta]\gamma\Theta_{CO}}{RT}\right) \tag{13}$$

The kinetic simulation parameters are adapted to test bench results of the HT-PEM fuel cell system that is operated on real syngas from the fuel processing system (Table 2).

Reference measurements of the cell voltage for carbon monoxide concentrations of 0.5% in the ATR syngas are compared with voltage measurements at higher carbon monoxide concentrations. The resulting voltage difference between the measurements is shown in Fig. 7. The HT-PEM simulation model enables a prediction of the carbon monoxide influence on the HT-PEM voltage for a wide range of temperatures and current densities.

3.2. ATR simulation

For the concentration and temperature profile simulation of the autothermal reformer and the watergas shift stages, one-dimensional, quasi-stationary reactor models are developed based on the conservation equations for mass and energy. The monolithic catalysts are subdivided into discrete volume elements, for which the concentration and temperature dependent reaction rates are determined.

For the kinetic simulation of the autothermal reformer, the reaction mechanisms for total oxidation (14), steam reforming (15) and watergas shift reaction (16) are considered.

$$CH_4 + 2O_2 \xrightarrow{r_{TOX}} CO_2 + 2H_2O \tag{14}$$

$$CH_4 + H_2O \xleftrightarrow{r_{SR1}} CO + 3H_2 \tag{15}$$

$$CO + H_2O \xleftrightarrow{r_{WGS}} CO_2 + H_2 \tag{16}$$

The approach of Trimm and Lam [12] is used for the total oxidation reaction of methane. For the steam reforming reaction and the watergas shift reaction rate equations from Numaguchi and Kikuchi [13] are adapted.

$$r_{TOX} = \frac{k_{TOX1}p_{CH_4}p_{O_2}}{(1+K^{ox}_{CH_4}p_{CH_4}+K^{ox}_{O_2}p_{O_2})^2} + \frac{k_{TOX2}p_{CH_4}p_{O_2}}{(1+K^{ox}_{CH_4}p_{CH_4}+K^{ox}_{O_2}p_{O_2})} \tag{17}$$

Table 2
Kinetic parameters of the HT-PEM simulation.

	Literature data [10,11]	HT-PEM simulation, adapted to testbench data
H_2 adsorption		
$k^{\circ}_{H,ads}$ ($m\,s^{-1}$)	29.8	29.8
$E^{k}_{H,ads}$ ($kJ\,mol^{-1}$)	10.4	11.7
H_2 desorption		
$b^{\circ}_{H,ads}$ ($\times 10^{11}\,mol\,m^{-3}$)	4.18	4.18
$E^{b}_{H,ads}$ ($kJ\,mol^{-1}$)	87.9	87.9
H_2 electrooxidation		
$k^{\circ}_{H,ox}$ ($mol\,m^{-2}\,s^{-1}$)	23.1	28.1
$E^{k}_{H,ox}$ ($kJ\,mol^{-1}$)	16.7	10.0
α_H (–)	0.5	0.5
CO adsorption		
$k^{\circ}_{CO,ads}$ ($\times 10^{4}\,m\,s^{-1}$)	3.01	3.01
$E^{k}_{CO,ads}$ ($kJ\,mol^{-1}$)	47.3	47.3
β (–)	0.1	0.1
γ ($kJ\,mol^{-1}$)	<100 °C: 39.7 100–115 °C: 41.4 >115 °C: 56.5	135 °C: 61.6 145 °C: 63.6 150 °C: 65.5 155 °C: 67.8 160 °C: 70.6
CO desorption		
$b^{\circ}_{CO,ads}$ ($\times 10^{3}\,mol\,m^{-3}$)	6.87	6.87
$E^{b}_{CO,ads}$ ($kJ\,mol^{-1}$)	100	100
CO electrooxidation		
$k^{\circ}_{CO,ox}$ ($\times 10^{12}\,mol\,m^{-2}\,s^{-1}$)	3.4	3.4
$E^{k}_{CO,ox}$ ($kJ\,mol^{-1}$)	127.0	170.0
α_{CO} (–)	0.5	0.5

$$r_{WDR1} = p_{CH_4}^{-\alpha_{WDR1}} p_{H_2O}^{-\beta_{WDR1}} k_{WDR1} \left(p_{CH_4} - \frac{(p_{H_2}^3 p_{CO})}{(p_{H_2O} K_{eq,WDR1})} \right) \quad (18)$$

$$r_{WGS} = p_{H_2O}^{-\beta_{WGS}} k_{WGS} \left(p_{CO} - \frac{(p_{H_2} p_{CO_2})}{(p_{H_2O} K_{eq,WGS})} \right) \quad (19)$$

The kinetic parameters for the rate equations are determined through detailed temperature measurements within the monolithic catalyst (Table 3).

Fig. 8 shows the measured and simulated temperature profile of the autothermal reformer. At the catalyst inlet, high reaction rates of the exothermal partial oxidation reaction result in a steep increase in catalyst temperature. The superposition of the endothermal steam reforming reaction with lower reaction rates yields a temperature maximum in the foremost part of the ATR catalyst. With the validated simulation model, the gas concentration profiles within the catalyst can be determined as well, enabling an optimized catalyst dimensioning.

One of the main influencing factors on catalyst degradation is the maximum catalyst temperature, which depends on inlet temperature, air/fuel ratio and steam/carbon ratio of the fuel processing system. The simulation model enables an accurate prediction of the maximum catalyst temperature within ±10 K for the investigated operating range of the ATR (χ_{ref} = 1.8–3.0, λ_{ref} = 0.22–0.30; Fig. 9).

Due to the integration of the offgas burner heat for educt preheating of the fuel processor, high conversion efficiencies of up to 85% from methane to hydrogen are achieved with the autothermal fuel processor.

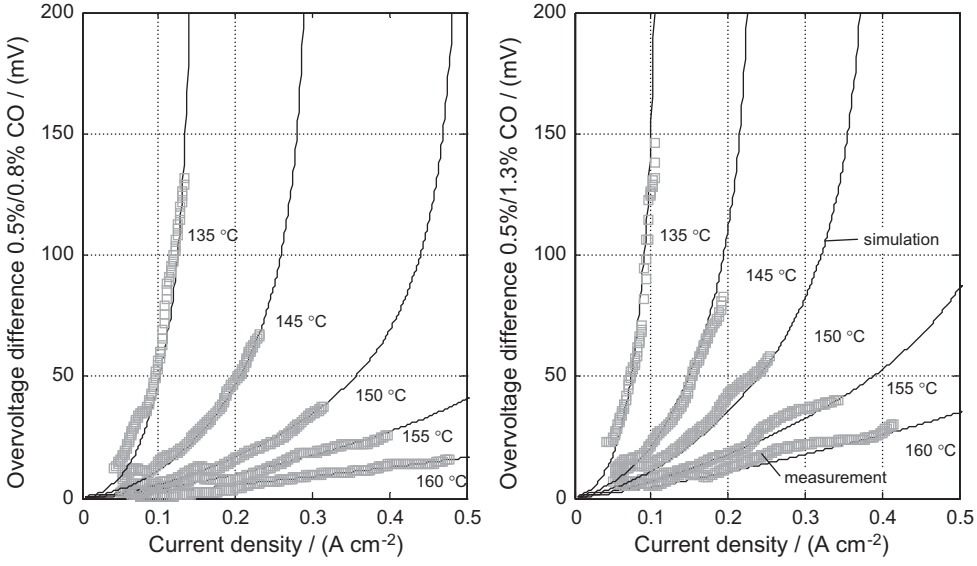

Fig. 7. Influence of CO concentration on the anodic overpotential – comparison of measurement and simulation (H_3PO_4/PBI membrane, 1 bar abs., reformate/air).

Table 3
Kinetic parameters of the ATR simulation.

	Literature data [14,15]	ATR simulation, adapted to testbench data
Total oxidation reaction		
k°_{TOX1} ($\times 10^{11}$ mol bar^{-2} kg$_{cat}^{-1}$ s^{-1})	8.11	10.11
$E_{a,TOX1}$ (kJ mol^{-1})	86.00	79.50
k°_{TOX2} ($\times 10^{5}$ mol bar^{-2} kg$_{cat}^{-1}$ s^{-1})	6.12	6.82
$E_{a,TOX2}$ (kJ mol^{-1})	86.00	79.50
$K^{ox,\circ}_{CH_4}$ (bar^{-1})	1.26	1.26
$\Delta H^{\circ}_{CH_4}$ (kJ mol^{-1})	−27.30	−27.30
$K^{ox,\circ}_{O_2}$ (bar^{-1})	7.87	7.87
$\Delta H^{\circ}_{O_2}$ (kJ mol^{-1})	−92.80	−92.80
Steam reforming reaction		
k°_{WDR1} ($\times 10^{5}$ mol bar$^{-0,404}$ kg$_{cat}^{-1}$ s^{-1})	2.58	2.30
$E_{a,WDR1}$ (kJ mol^{-1})	106.90	91.00
α_{WDR1} (−)	0	0
β_{WDR1} (−)	0.596	0.596
Watergas-shift reaction		
k°_{WGS} ($\times 10^{2}$ mol bar^{-1} kg$_{cat}^{-1}$ s^{-1})	2.45	84.50
$E_{a,WGS}$ (kJ mol^{-1})	54.30	30.00
β_{WGS} (−)	0	0

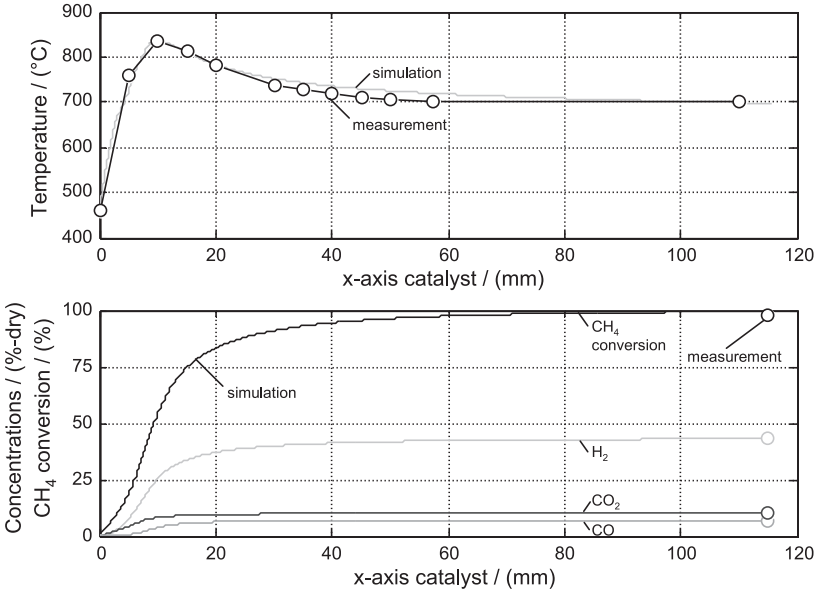

Fig. 8. Temperature and concentration profile of the autothermal reformer – comparison of measurement and simulation (ATR 46 mm × 46 mm × 115 mm, 900 CPSI, GHSV 72,000 h^{-1}, λ_{ref} = 0.3, χ_{ref} = 2.9).

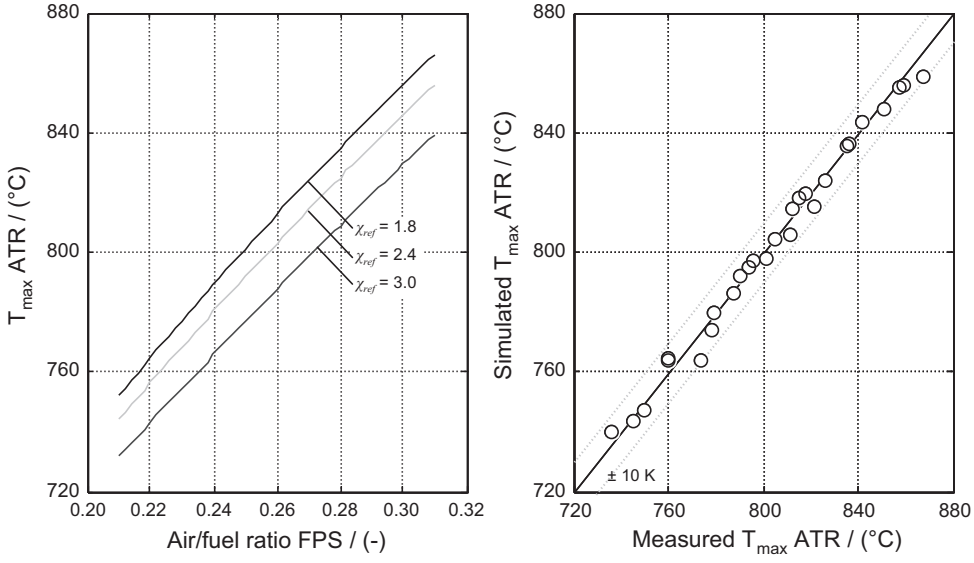

Fig. 9. Influence of the air/fuel ratio and the steam/carbon ratio of the fuel processing system on the maximum reactor temperature – measurement and simulation (educt temperature 450 °C).

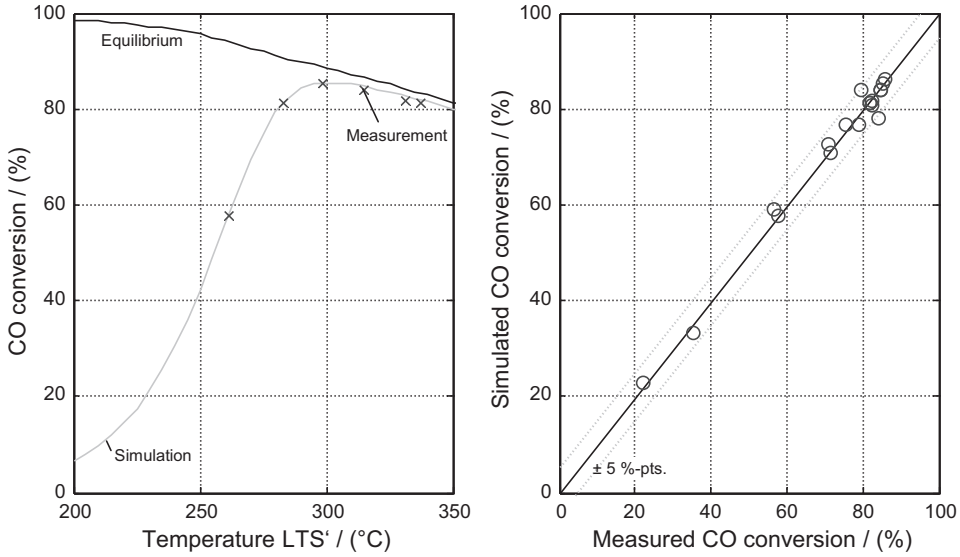

Fig. 10. Temperature influence on the CO conversion rate of the low temperature shift – comparison measurement and simulation (GHSV 10,000 h^{-1}, 1 bar abs., $\lambda_{ref} = 0.28$, $\chi_{ref} = 2.5$).

3.3. WGS simulation

The reaction rate in the WGS reactors, at significantly lower temperatures compared to the autothermal reformer, can be approximated by the following power law [16]:

$$r_{WGS} = \left(1 - \frac{p_{CO_2} p_{H_2}}{p_{CO} p_{H_2O} K_{eq,WGS}}\right) p_{CO}^{\alpha} p_{H_2O}^{\beta} p_{CO_2}^{\gamma} p_{H_2}^{\delta} k_a \quad \exp\left(\frac{-E_a}{R_m T}\right) \tag{20}$$

Simulation results of the carbon monoxide conversion within the low temperature shift reactor are in agreement with testbench data (Fig. 10). The high temperature shift inlet temperature profile varies significantly across the catalyst, so that the CO conversion rates cannot be predicted within the 1D simulation. Modifications of the heat exchanger upstream of the high temperature shift allow for a more homogenous temperature distribution and a decrease of the reactor volume in future development stages.

4. DOE optimization of the APU system

In order to optimize the global system parameters cathode stoichiometry, anode stoichiometry as well as air/fuel ratio and steam/carbon ratio of the fuel processing system for all system operating points, the simulation models of ATR, WGS and HT-PEM are combined in an overall system model. The influence of additional operating parameters and the required input power for auxiliary components is incorporated in performance maps that are based on testbench data. Design of experiments (DOE) is used to generate cubic polynomial models of all system output parameters. The polynomial models enable the constrained optimization of the system efficiency as a function of net system power for defined

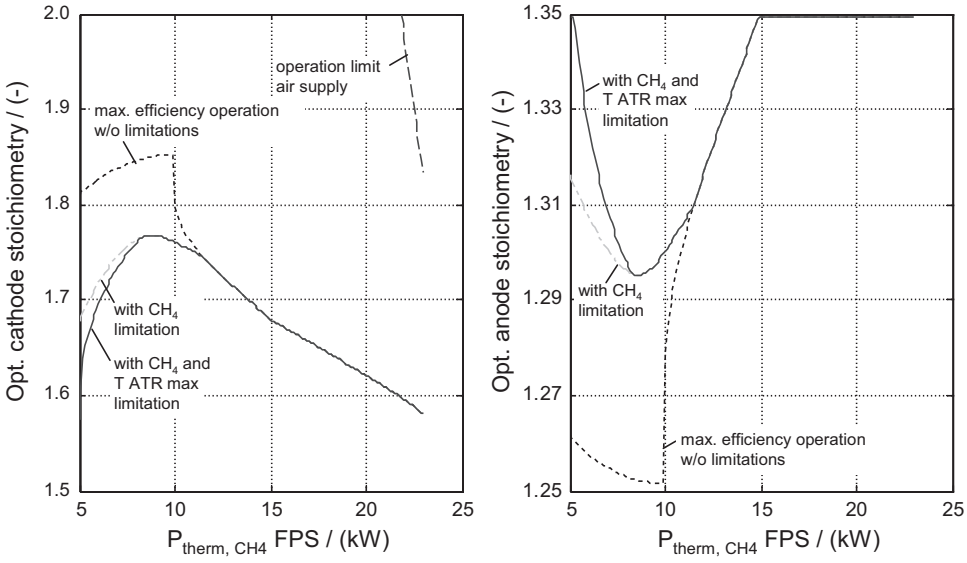

Fig. 11. DOE optimization of stack parameters for max. system efficiency.

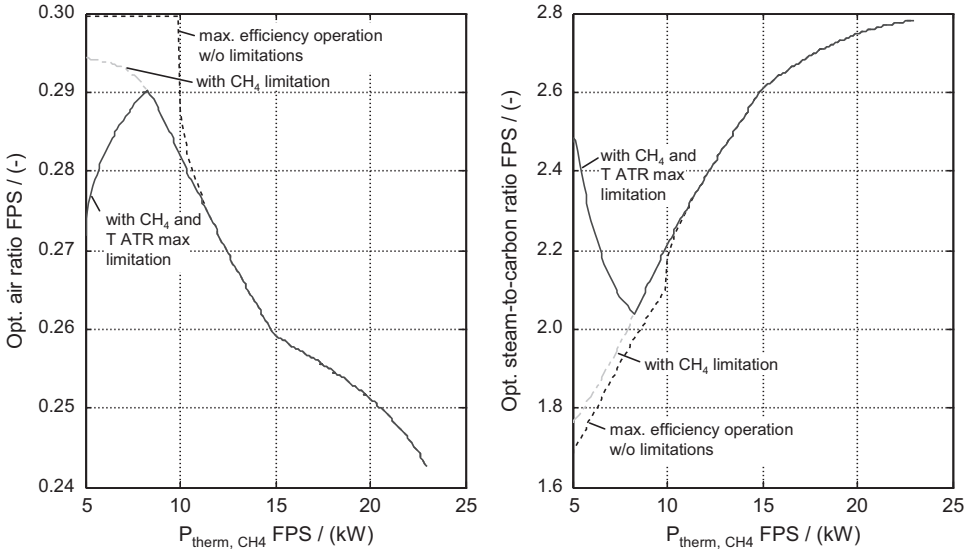

Fig. 12. DOE optimization of fuel processing system parameters for max. system efficiency.

boundary conditions (temperatures, emissions, operating boundaries of subsystems).

Figs. 11 and 12 show the combinations of the global system parameters for which maximum system efficiencies are achieved (· · · · · · · · dotted line). All four global system parameters are optimized simultaneously. At high loads and, thus, high current densities, increased anode stoichiometries enable significant efficiency advantages of the HT-PEM fuel cell stack. Furthermore, the higher percentage of hydrogen that is converted in the offgas burner enables a reduction of the required air/fuel ratio of the fuel processing system. In order to realize low carbon monoxide concentrations at high space velocities within the watergas shift stages, the steam/carbon ratio is increased. The cathode stoichiometry is decreased because the moderate rise in cell voltage, with increasing cathode massflow, is overcompensated by the higher power requirement of the air supply system.

For low system power outputs and low current densities, the influence of the anode stoichiometry on stack efficiency decreases, and therefore, the highest system efficiencies are reached for low anode stoichiometries. Due to reduced temperatures of the offgas burner, the air/fuel ratio of the fuel processor has to be increased in order to ensure adequate temperatures and methane conversion rates within the autothermal reformer.

In addition to high system efficiencies, exhaust emissions and maximum component temperatures can be defined as constraints in the optimization of the global system parameters. For the HT-PEM fuel cell APU system, methane emissions increase at low system loads for maximum efficiency operation, due to low anode stoichiometries, and thus, reduced offgas burner temperatures and resulting low methane conversion rates (Fig. 13, dotted line). In a second optimization step the methane emissions are limited to 100 mg kWh_{el}^{-1}, resulting in the change of the global system parameters shown in Figs. 11 and 12 (— · — dashed-dotted line).

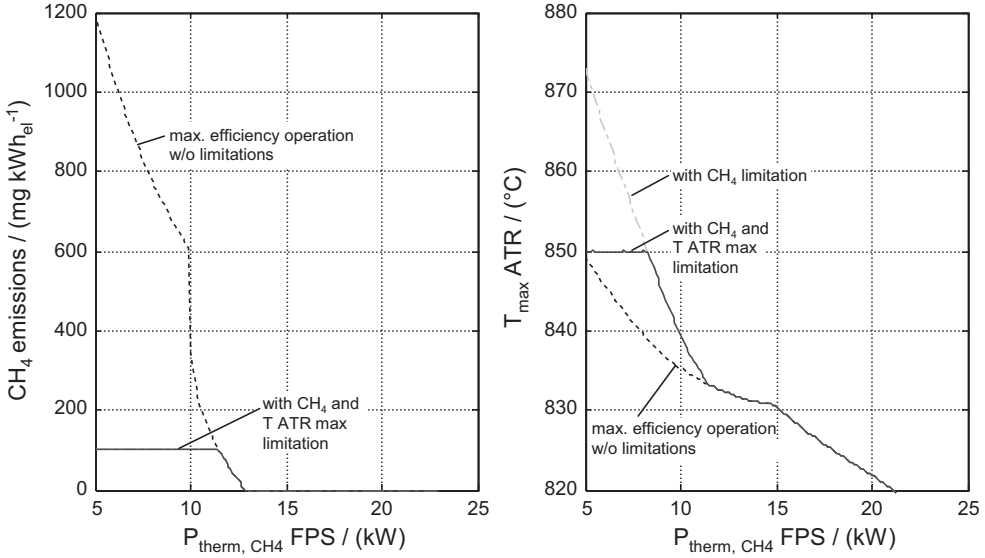

Fig. 13. DOE simulation methane emissions and max. ATR temperature.

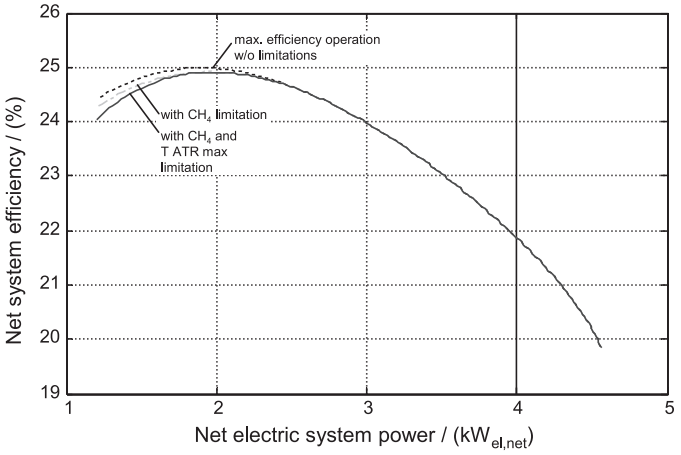

Fig. 14. DOE optimization of net system efficiency.

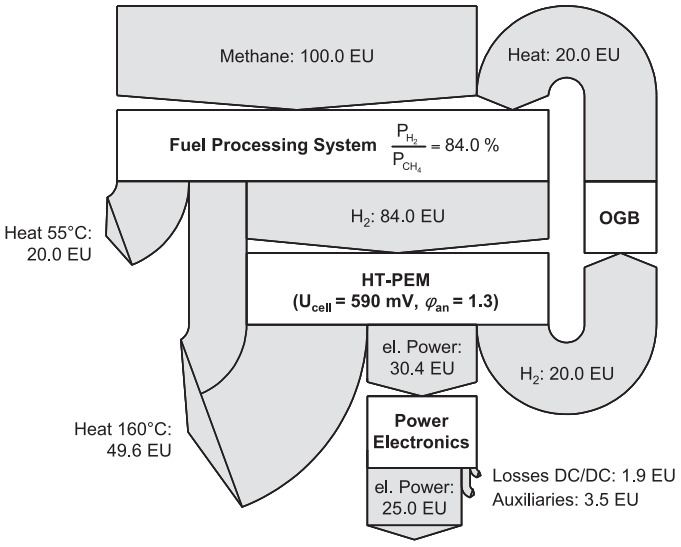

Fig. 15. Sankey diagram of the HT-PEM fuel cell system in part load operation ($2\,kW_{el,net.}$).

Temperature and methane conversion rate of the offgas burner are increased due to higher anode stoichiometries and lower cathode stoichiometries. In a third optimization step, the air/fuel ratio of the fuel processing system is decreased and the steam/carbon ratio is increased in order to limit the maximum ATR temperature to 850 °C and reduce catalyst degradation (Figs. 11–13, —— solid line).

Fig. 14 shows the resulting, optimized net system efficiency as a function of net system electric power output for all three optimization steps. Maximum system efficiencies of 25% are reached with the HT-PEM APU prototype for a net system power output of 2 kW. For nominal load, a reduced fuel cell stack efficiency at high current densities results in a total system efficiency of 20%. At low partload system efficiency also decreases due to a disproportionate increase of the auxiliary components' power requirement. The additional boundary conditions regarding methane emission-/maximum ATR temperature limitations have only a minor effect of less than 0.5 percentage points in the lowest partload range.

A sankey diagram for part load operation is shown in Fig. 15. In order to increase the overall system efficiency, the fuel cell stack has the largest optimization potential. For the prototype, a cell voltage of 500–550 mV is achieved at nominal load, anode stoichiometries of >1.25 are required. An increase in power density and cell voltage will significantly improve overall system efficiency. Further optimization potential can be realized by increasing the fuel processing system efficiency and reducing the power consumption of the auxiliaries.

5. Conclusion

In this work, the concept development, system layout, component simulation and overall DOE system optimization of a HT-PEM fuel cell APU with onboard fuel processor have been presented. The HT-PEM fuel cell has the benefits of an improved thermal cyclability, shorter startup times and a higher resistance against vibrations compared to solid oxide fuel cells. Compared to LT-PEM fuel cell systems with onboard fuel processor, the system complexity can be significantly reduced. An ATR fuel processing system was selected due to transient performance advantages compared to steam reformers and reduced catalyst degradation and soot formation tendency compared to partial oxidation reactors. A low pressure air supply system was chosen because of low noise emissions, system complexity and system cost.

A highly integrated system layout has been developed that enables fast startup within 7.5 min, a closed system water balance and high fuel processor efficiencies of up to 85% (ATR methane-to-hydrogen conversion efficiency without balance of plant components) due to the recuperation of the anode offgas burner heat. The integration of the system battery into the load management enhances the transient electric performance and the maximum electric power output of the APU system.

Simulation models have been developed for the HT-PEM fuel cell, the autothermal reformer and the watergas shift stages. They enable the prediction of the carbon monoxide influence on cell voltage, a detailed analysis of the ATR reactor temperature and concentration profiles for optimized catalyst dimensioning, and prevention of degradation due to catalyst overheating. With the WGS simulation, the shift stage operating temperatures can be optimized in order to achieve maximum carbon monoxide conversion rates.

Design of experiments has been used to generate cubic polynomial models of all system output parameters. Based on these models, the four global system parameters cathode stoichiometry, anode stoichiometry, air/fuel ratio and steam/carbon ratio of the fuel processing system could be optimized for all system operating points. Boundary conditions as methane conversion rates of the offgas burner or maximum component temperatures were incorporated in the optimization.

In order to increase overall system efficiency of the HT-PEM fuel cell APU prototype, the fuel cell stack has the largest optimization potential. An increase in fuel processing system efficiency and a reduced power consumption of the auxiliaries will enable further efficiency gains. Additionally, with a design optimization of the system components a reduction of overall system weight and shorter system startup times due to lower thermal inertias of the stack and the fuel processor can be achieved.

Acknowledgement

The authors gratefully acknowledge the financial support of the German Federal Ministry of Economics and Technology based on a decision of the German Bundestag (research grant FKZ 0327728A and FKZ 0327777P). The authors are responsible for the content of the publication.

Appendix A.

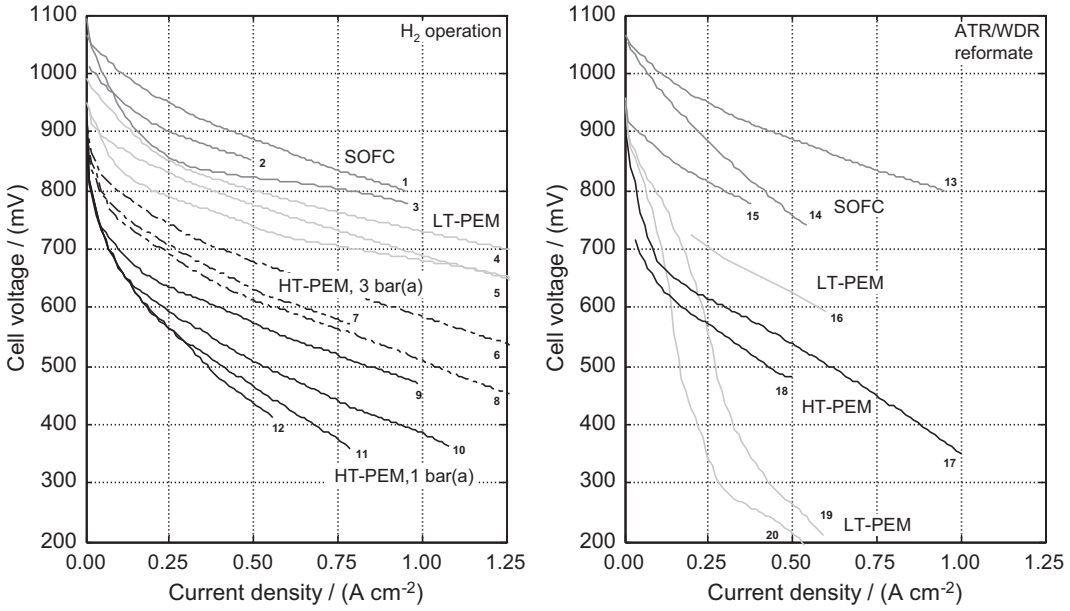

	Anode	CO / (ppm)	Cathode	Pressure / (bar)	Temp. / (°C)	φ_{An}	λ_{Cat}	Source
1	48.5 % H_2, 3 % H_2O				750-825			[17]
2	H_2, N_2		air		725	4.30	3.6	[18]
3	H_2		air		675	2.20	2.8	[19]
4	H_2		air	1.5	65	1.50	2.0	[20]
5				1.0	80			[21]
6	H_2		air	3.0	160			[22]
7	H_2		air	3.0	160			[23]
8	H_2		air	3.0	160			[24]
9	H_2		air	1.0	160			[25]
10	H_2		air	1.0	170			[26]
11	H_2		air	1.0	160			[24]
12	H_2		air	1.0	180			[27]
13	48.5 % H_2, 3 % H_2O				750-825			[17]
14	reformate		air		750			[28]
15	reformate, 50 % int. reforming		air		725	1.54	2.5	[29]
16	ATR reformate	5000	air	3,0	80	1.25		[30]
17	WDR reformate	10000	air	1.0	160	1.20	2.0	[31]
18	ATR reformate	7000	air	1.0	160	1.25	2.5	
19	H_2	100	O_2	2.2/2.4	80			[32]
20	H_2	250	O_2	2.2/2.4	80			[32]

Fig. 16. Current/voltage characteristics of different LT-PEM, HT-PEM and solid oxide fuel cells for hydrogen operation and ATR/WDR reformate operation (curve 18: own data).

References

[1] N. Jalani, M. Ramani, K. Ohlsson, S. Buelte, G. Pacifico, R. Pollard, R. Staudt, R. Datta, Journal of Power Sources 160 (2) (2006) 1096–1103.
[2] J. Zhang, Y. Tang, C. Song, J. Zhang, Journal of Power Sources 172 (2007) 163–171.
[3] J. Baschuk, X. Li, International Journal of Energy Research 25 (2001) 695–713.
[4] T. Springer, T. Zawodzinski, S. Gottesfeld, Proceedings of the Symposium on Electrode Processes for Energy Conversion and Storage IV, 1998.
[5] J. Hyunchul, K. Lee, U. Sukkee, Journal of Mechanical Science and Technology 22 (2008) 991–998.
[6] A. Rodrigues, J. Amphlett, R. Mann, B. Peppley, P. Roberge, Proceedings of the 32nd Intersociety Energy Conversion Engineering Conferernce, vol. 2, 1997, pp. 768–773.
[7] R. Bellows, E. Marucchi-Soos, D. Buckley, Industrial & Engineering Chemical Research 35 (1996) 1235–1242.
[8] J.J. Baschuk, X. Li, International Journal of Global Energy Issues 20 (3) (2003) 245–276.
[9] X. Li, Presentation at the Computational Fuel Cell Dynamics Workshop, vol. 1, Banff International Research Station, April 19–25, 2003.
[10] A. Bergman, D. Gerteisen, T. Kurz, Fuel Cells 00 0 (2009) 1–10.
[11] J. Baschuk, X. Li, International Journal of Energy Research 27 (2003) 1095–1116.
[12] D. Trimm, C. Lam, Chemical Engineering Science 35 (1980) 1405–1413.
[13] T. Numaguchi, K. Kikuchi, Chemical Engineering Science 43 (1988) 2295–2301.
[14] C. de Smet, Partial oxidation of methane to synthesis gas: reaction kinetics and reactor modelling; Dissertation Technische Universität Eindhoven (2000).
[15] F. Gallucci, M. van Sint Annaland, J. Kuipers, Asia-Pacific Journal of Chemical Engineering 4 (2009) 334–344.
[16] C. Severin, Benzinbetriebenes Gaserzeugungssystem für die PKW-Bordstromversorgung auf PEM-Brennstoffzellenbasis; Dissertation RWTH Aachen (2006).
[17] R. Kerr, 2009 SECA Annual Review Meeting, 2009.
[18] B. Borglum, Proceedings of the Ninth International Symposium on Solid Oxide Fuel Cells (SOFC-IX), 2005.
[19] D. Norrick, Cummins Power Generation SECA Phase 1 Review, 2007.
[20] Ballard, Product Information AvCarb®EP40, EP40T, GDS3215 (D13), 2006.

[21] J. Köhler, Proceedings of the Fuel Cell Seminar 2003, 2003.
[22] R. Staudt, 2006 Annual Progress Report, 2006.
[23] G. Hübner, J. Huslage, F. Seyfried, Volkswagen Contribution to PBI Membranes and Fuel Cells, 2008.
[24] A. Reiche, Proceedings of the Fuel Cell Seminar 2006, 2006, abstracts 502 and 507.
[25] PEMEAS, Fuel Cell Bulletin 2006, vol. 2, 2006, pp. 12–15.
[26] Q. Li, J. Jensen, C. Pan, V. Bandur, M. Nilsson, F. Schönberger, et al., Fuel Cells 2008 8 (2008) 188–199.
[27] D. Stolten, C. Wannek, H. Dohle, L. Blum, J. Mergel, R. Peters, Proceedings of the Fuel Cell Seminar 2007 (2007), abstract 162.
[28] J. Bae, L. Sungkwang, H. Jee, J. Kim, Y. Yoo, T. Lee, Journal of Power Sources 172 (2007) (2007) 100–107.
[29] B. Borglum, Proceedings of the Fuel Cell Seminar 2006, 2006.
[30] S. Ball, Investigation of PEMFC MEAs for ultra-high CO reformate; Report DTI new and renewable energy programm, 2004 (F/02/00261/REP URN 04/558).
[31] I. Kundler, C. Henschel, APU Workshop 2005, Erlangen, 2005.
[32] H. Oetjen, V. Schmidt, U. Stimming, F. Trila, Journal of the Electrochemical Society 143 (1996) 3838–3842.

Glossary of terms

Symbols

b: reaction rate constant, various (depending on reaction equation)
c: concentration, kmol m^{-3}
c_p: specific heat capacity at constant pressure, kJ (kg K)$^{-1}$
E_a: activation energy, kJ
F: Faraday's-constant, As mol^{-1}
i: current density, A cm^{-2}
I: current, A
k: reaction rate constant, various (depending on reaction equation)
K: equilibrium constant, –
$\dot{m}$: massflow, kg s^{-1}
M: molar mass, kg kmol^{-1}
$\dot{n}$: molar flow, kmol s^{-1}
p, p_i: pressure, partial pressure, bar
Δp: differential pressure, bar
P: power, kW
r: reaction rate, kmol (s kg$_{cat}$)$^{-1}$
R: universal gas constant, kJ (kmol K)$^{-1}$
T: temperature, K
U: voltage, V
x: number of carbon atoms within the hydrocarbon molecule, –
x: number of cells in the fuel cell stack, –
y: number of hydrogen atoms within the hydrocarbon molecule, –

Greek symbols

α: symmetry factor, –
α, β, γ, δ: exponents of reaction rate equation, –
β: symmetry factor, –
γ: interaction parameter CO-adsorption, kJ mol^{-1}
Δ: difference, –
ζ: conversion rate, –
η: efficiency, –
η_{ref}: fuel processing system efficiency, –
Θ: surface coverage, –
κ: isentropic exponent, –
λ_{ref}: air/fuel ratio fuel processing system, –
λ_{cat}: cathode stoichiometry, –
ξ: mass fraction, kg$_i$ kg^{-1}
Π: pressure ratio air supply system, –
φ_{an}: anode stoichiometry, –
χ_{ref}: steam/carbon ratio fuel processing system, mol$_{H_2O}$ mol$_C^{-1}$
ψ_i: molar fraction, mol$_i$ mol^{-1}

Indices

a: activation
ads: adsorption
amb: ambient
an: anode
comp: compressor
exh: exhaust
FB: flame burner
i: component i
cat: catalyst
cath: cathode
m: molar
max: maximum
min: minimum
ox: oxidation
Ref: reformer
SR: steam reforming
st: stoichiometric
Sta: stack
TOX: total oxidation
WGS: watergas-shift

Abbreviations

APU: auxiliary power unit
ATR: autothermal reforming
CB: catalytic burner
CPSI: cells per square inch
DOE: design of experiments
FPS: fuel processing system
GHSV: gas hourly space velocity
HT: high temperature
HTS: high temperature shift
LT: low temperature
LTS: low temperature shift
MEA: membrane electrode assembly
NVH: noise, vibration and harshness
OGB: offgas burner
PEM: proton exchange membrane
CPO: catalytic partial oxidation
SOFC: solid oxide fuel cell
SR: steam reforming